Pharmaceutical Sciences and Drug Design
ISSN: 3062-4428
2026, Volume 6, Issue 1, Page No: 266-288

Available online at: www.galaxypub.co/page/journals

Galaxy Publication

Additively Manufactured Plasmonic Platforms for Light-Triggered and Programmable Drug Release

Claire Dupont[1]*, Julien Martin[1]

[1]Department of Pharmaceutical Sciences and Drug Research, Faculty of Pharmacy, University of Bordeaux, Bordeaux, France.

* **E-mail** ✉ claire.dupont@gmail.com

Received: 09 March 2026; **Revised:** 03 June 2026; **Accepted:** 07 June 2026

ABSTRACT

Gold nanoparticles possess the capacity to convert incident radiation into thermal energy through plasmonic effects, a behavior modulated by both particle size and geometry. This intrinsic property enables the spatiotemporal orchestration of active payload release from polymer-based pharmaceutical carriers, thereby reducing undesirable side reactions and unintended leakage. Three-dimensional printing, specifically the vat photopolymerization modality, has emerged as a powerful fabrication route for incorporating nanoparticulate components into architecturally sophisticated dosage forms. The present investigation aimed to embed gold nanospheres (AuNSs) and nanorods (AuNRs) within photocrosslinked polymeric scaffolds via vat photopolymerization, enabling externally regulated drug elution upon irradiation with 532 nm and 1064 nm light. Niclosamide (Lot 0000122971), Polyethylene glycol diacrylate with a molecular weight of 250 (PEGDA 250), Polyethylene glycol with a molecular weight of 400 (PEG 400), as well as diphenyl (2,4,6-trimethylbenzoyl) phosphine oxide (TPO) as the radical photoinitiator, were all purchased from Sigma-Aldrich (St. Louis, MO, USA). Milli-Q ultrapure water, with a resistivity of 18.2 MΩ at 25 °C and filtered through a 0.22 µm membrane, was used in all experimental procedures. Except for explicitly stated cases, all other reagents and solvents were of analytical-grade purity. Statistical evaluation and graphical representation were performed using GraphPad Prism version 7.0 (GraphPad Software, San Diego, CA, USA). The AuNSs (27 nm diameter) displayed photo-responsiveness to 532 nm, whereas the AuNRs (measuring 60 nm in length and 10 nm in width) were activated by 1064 nm. Niclosamide was employed as the model therapeutic payload. Ternary formulations consisting of Polyethylene Glycol Diacrylate 250 (PEGDA 250), Polyethylene Glycol 400 (PEG 400), and water were systematically refined through DesignExpert 11 software to achieve irradiation wavelength-selective release kinetics. Three printable matrices, shortlisted according to solubility and fabrication fidelity, were subjected to exhaustive physicochemical profiling. Of these, two compositions successfully demonstrated gated drug liberation tuned to specific optical wavelengths. Bilayer architectures integrating both AuNSs and AuNRs within discrete compartments exhibited wavelength-discriminating drug release behavior. A light-activatable pharmaceutical construct was successfully engineered, capable of modulating drug output in direct response to optical stimulation, with translational promise for therapeutic regimens where deferred or pulsatile administration is clinically indicated.

Keywords: 3D printing, Controlled drug release, Photothermal drug delivery, Niclosamide, Vat photopolymerization

How to Cite This Article: Dupont C, Martin J. Additively Manufactured Plasmonic Platforms for Light-Triggered and Programmable Drug Release. Pharm Sci Drug Des. 2026;6(1):266-88. https://doi.org/10.51847/klvdltg1Q5

Introduction

For a pharmaceutical compound to achieve its intended therapeutic outcome, it must bind its molecular target and trigger the desired biological cascade. The fundamental aim of any formulated medicinal product is to provide both safe and efficacious drug delivery, maintaining plasma levels within the therapeutic range while avoiding concentrations that encroach on toxicity [1].

The inherent limitation of classical drug delivery platforms is their tendency to disseminate an active agent throughout the entire systemic circulation rather than confining its distribution to the anatomical compartment

requiring pharmacological intervention. This indiscriminate biodistribution becomes clinically consequential when the drug impacts off-target organs or tissues, eliciting unwanted effects. To compensate, large and frequently repeated doses become necessary to guarantee that a sufficient fraction reaches the intended site, a practice that brings with it a suite of drawbacks, including the onset of adverse reactions, an elevated risk of cumulative toxicity, and a marked deterioration in the patient's overall wellbeing [2].

The paradigm of directing therapeutic molecules toward a preselected locus of action was conceived specifically to overcome the foregoing limitations. This conceptual evolution spurred the development of varied strategies encompassing both administration routes and engineered dosage forms for conveying bioactive molecules. A formulated product dictates key biopharmaceutical determinants, such as the underlying release mechanism, which in turn govern the drug's systemic availability and ultimate potency [3, 4]. Modified-release systems allow the formulator to control liberation kinetics and, consequently, the temporal persistence of the drug within the body. Furthermore, delivery systems can be architecturally customized to unload their cargo at predetermined spatiotemporal coordinates, ensuring that the active moiety encounters its pharmacological site of action at the optimal moment [5].

Among the most revolutionary methodologies for molecular steering, or vectorization, is nanotechnology. Shrinking particulate entities down to the nanometer regime unlocks several advantages, most notably a dramatically enlarged surface-to-volume ratio that greatly facilitates the surface engineering and decoration of nanoparticles [6, 7]. This architectural feature permits the covalent or non-covalent tethering of targeting ligands, thereby enabling site-selective homing. Additionally, because of their diminutive size, the dissolution kinetics of poorly water-soluble pharmaceuticals are accelerated, enhancing their oral bioavailability and their passage across physiological membrane barriers [8].

An expansive repertoire of materials exists for nanoparticle construction, spanning both organic and inorganic chemical space. Organic nanosystems embrace micellar constructs, liposomal vesicles, polymeric nanocapsules, dendrimeric scaffolds, and solid polymeric particulates [9]. The inorganic domain covers metallic elements such as copper, silver, iron, silicon dioxide, and gold. These elemental building blocks can be sculpted into a rich diversity of morphologies and dimensions, including spheres, rods, prisms, and stellated shapes. In addition, metallic nanomaterials exhibit optical and magnetic phenomena arising from the coupling of nanoparticles with electromagnetic fields [10]. Gold, in particular, receives special attention owing to its favorable biocompatibility profile, negligible cytotoxic burden, remarkable chemical resilience conferred by gold–thiol coordination chemistry, and synthetic tractability. The convergence of all these attributes renders gold nanoparticles exceptionally well-suited candidates for biomedical deployment [11].

Gold nanoparticles (AuNPs) display pronounced optical and magnetic signatures arising from the high density of conduction-band electrons on their surfaces, enabling unrestricted electron mobility. Localized surface plasmon resonance (LSPR) describes the coherent, phase-matched collective oscillation of these outermost conduction electrons when confined within a metallic nanostructure [12]. The resonant oscillation is triggered and sustained by the electromagnetic stimulus of incident light, as depicted schematically in **Figure 1**. This light–matter coupling results in markedly intensified localized energy conversion, which, in the specific case of gold nanoparticles, translates into a pronounced photothermal output [13].

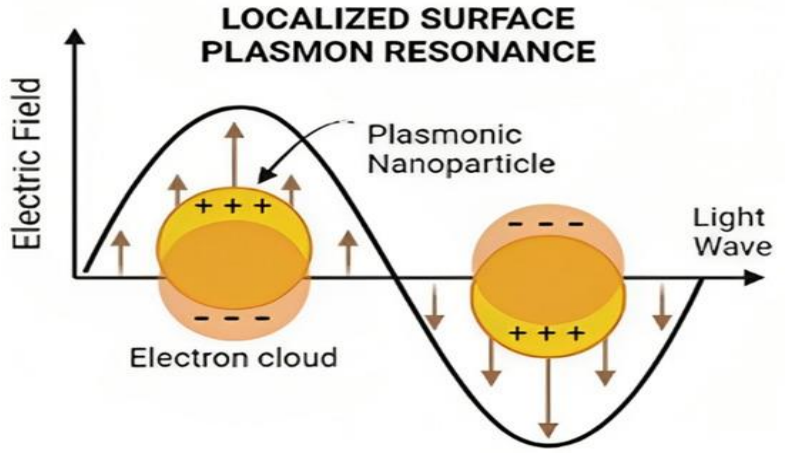

Figure 1. Schematic representation of localized surface plasmon resonance.

The dimensional and geometric characteristics of the nanoparticle directly influence the energy threshold required to initiate LSPR [14]. This size- and shape-dependence arises because the physical boundaries of the nanostructure constrain the available degrees of freedom for electron motion. When the electron population housed within the nanostructure is larger—as encountered in nanorods endowed with extended surface areas—the resonance band is appreciably broadened, meaning that less energetic photons are sufficient to couple with and excite these electrons [15]. Larger nanoparticles thus require lower photon energies, manifesting experimentally as absorption bands at longer wavelengths, in accordance with the inverse energy–wavelength relationship. This physical basis explains why the plasmon absorption of gold nanorods is centered near 1064 nm, whereas that of smaller gold nanospheres, with their comparatively smaller surface areas, appears near 520 nm. The plasmonic signatures of these nanoparticulate systems hold immense practical value for targeted drug delivery, remotely gated cargo release, and photothermally mediated therapeutic regimens [16].

A significant impediment to translating nanoparticles into pharmaceutical formulations is their incorporation into solid constructs while preserving their distinctive characteristics. A trailblazing solution to this predicament is 3D printing. This additive fabrication technology constructs solid, three-dimensional artifacts directed by digital instructions [17, 18].

At its core, 3D printing enables the generation of solid bodies across a wide spectrum of dimensions and configurations, achieving exacting levels of personalization. It enables the combination of materials with vastly different physicochemical properties and resin formulations containing multiple bioactive compounds or nanomaterial cargoes [19]. These may be positioned selectively in discrete printed strata or on distinct faces without blending. The technology enables the fabrication of unconventional geometries that evade traditional manufacturing paradigms, such as hollow interiors or porous lattices.

Among the suite of 3D-printing modalities, VAT photopolymerization (VATp) is particularly prominent. It covers a range of processes that rely on liquid resin baths that solidify via photoinitiated polymerization upon exposure to light. The most common VATp setup involves decanting a photocurable resin into a container. As fabrication begins, the build stage is lowered into the liquid resin reservoir, leaving a thin film of fluid sandwiched between the stage and the container floor. A UV laser beam then scans a two-dimensional slice of the digital model, hardening the resin selectively. The process is inherently incremental, progressing one layer at a time. Once a segment is finalized, the platform lifts, enabling fresh resin to flow into place and ready the surface for the subsequent deposition cycle [20].

Printable feedstocks include photosensitive macromonomers, such as polyethylene glycol diacrylate (PEGDA) of varying chain lengths and polyethylene glycol (PEG), and radical photoinitiators, such as acylphosphine oxide derivatives [21, 22]. VATp offers clear benefits over alternative technologies, including outstanding fabrication resolution and fidelity. Its versatility is demonstrated by its capacity to formulate a wide range of photocurable liquid systems that can dissolve a broad array of molecular entities, including therapeutic agents and nanosized fillers, within the liquid phase. Equally appealing is the technique's ability to achieve rapid throughput at ambient temperature.

The convergence of plasmonic nanoparticles with additive manufacturing exploits the above-described merits, generating synergy between the geometric exactitude inherent to three-dimensional construction, the potential for bespoke customization, the amalgamation of disparate functional materials within a single printed entity, and the optical and magnetic responses of plasmonic nanomaterials.

Stimuli sensitivity is critical for directing the release kinetics of a drug from a carrier or a 3D-printed medicinal platform. Endogenous cues consist of pH gradients, ionic strength variations, and enzymatic turnover, though these biochemical parameters are often subject to patient-specific variability [23]. Exogenous cues, among which light is a prime example, remain decoupled from the subject's internal physiological state. This investigation, therefore, probes the incorporation of gold nanospheres and nanorods into polymer networks formed via VATp 3D printing.

Accordingly, the ambition was to architect a polymer-based pharmaceutical construct capable of dictating the outflow of an active principle via irradiation at wavelengths near the near-infrared (NIR) plasmon resonance. Among the envisioned applications for this technology is the capacity to generate multi-pulse dosing platforms suited to the management of long-term illnesses such as malignant disease, where an upfront loading dose followed by protracted maintenance dosing is clinically warranted. It can also be deployed in regimens that require the delivery of two distinct therapeutic entities, as exemplified by post-operative management, where a single device activated by light could sequentially release an analgesic bolus and an antibiotic dose following a single

application. The solubility and likely therapeutic indication of a model compound guided the design of the proposed platform. Niclosamide (NICLO), a salicylic acid congener, falls under class II of the Biopharmaceutical Classification System (BCS), characterized by poor aqueous solubility and high membrane permeability. Originally marketed as an anthelmintic targeting tapeworms within the genus Taenia, its mode of action relies on uncoupling oxidative phosphorylation in the parasite. Today, Niclosamide is undergoing repurposing evaluation, with reported effectiveness against gastric, prostate, and breast malignancies. It has also shown beneficial activity in the context of COVID-19 and Helicobacter pylori infection [24]. In essence, the formulation design was constructed around the dissolution characteristics of the model agent and its intended liberation behavior. This architectural blueprint can consequently be extrapolated for the delivery of other drug molecules belonging to alternative BCS categories.

Thus, the overarching aim of this study was to conceive, produce, and thoroughly characterize 3D-printed constructs destined for photothermal therapy. It united VATp with gold nanoparticles to orchestrate the on-demand release of the model drug, building on bilayer configurations that merge nanospheres and nanorods and showcasing the capacity for wavelength-selective, spatially precise drug liberation contingent on the applied irradiation.

Materials and Methods

Materials

Niclosamide (Lot 0000122971), Polyethylene glycol diacrylate with a molecular weight of 250 (PEGDA 250), Polyethylene glycol with a molecular weight of 400 (PEG 400), as well as diphenyl (2,4,6-trimethylbenzoyl) phosphine oxide (TPO) as the radical photoinitiator, were all purchased from Sigma-Aldrich (St. Louis, MO, USA). Milli-Q ultrapure water, with a resistivity of 18.2 MΩ at 25 °C and filtered through a 0.22 µm membrane, was used in all experimental procedures. Except for explicitly stated cases, all other reagents and solvents were of analytical-grade purity.

Synthesis of gold nanoparticles of different morphologies

The preparative procedure was followed to generate gold nanospheres (AuNSs). Briefly, the AuNSs were produced through the citrate-driven reduction of $HAuCl_4$. An aqueous solution of $HAuCl_4$ was brought to a rolling boil and, after 10 min, a preheated (50–60 °C) aqueous sodium citrate solution (38.8 mM) was added. The reaction mixture was refluxed in a round-bottom flask for 30 min, at which point a deep ruby-red colloidal dispersion indicated the completion of nanoparticle formation. Once the AuNSs had been obtained, the pH was adjusted to 7–8 using a dilute NaOH solution [20].

Gold nanorods (AuNRs) were fabricated following an adapted seed-mediated growth methodology [25]. The seed suspension was prepared by mixing 85 µL of a $HAuCl_4$ stock solution (29.4 mM) with 4.915 mL of Cetyltrimethylammonium bromide (CTAB) solution (0.1 M) and stirring for 5 min. Afterward, 300 µL of an ice-chilled, freshly made $NaBH_4$/NaOH solution (10 mM/0.01 M) was dispensed into the vessel to reduce the gold salt chemically, and agitation was maintained for an additional 30 min. In a separate container, the growth medium was prepared by combining 170 µL of the $HAuCl_4$ stock (29.4 mM) with 9.83 mL of CTAB (0.1 M), then stirring for 10 min. Next, 1 mL of $AgNO_3$ solution (10 mM) was introduced and mixed for 30 s. After the lapse of this period, 500 µL of hydroquinone (100 mM) was added, and stirring was continued until a distinct color change (from yellow to colorless) was observed. Ultimately, 160 µL of the previously prepared seed colloid was added to the growth solution, and the combined mixture was stored undisturbed overnight to allow complete anisotropic growth [26].

Plasmon resonance assessment

The optical plasmonic signatures of the AuNSs and AuNRs were examined through UV–visible absorption spectroscopy using an Agilent 8453 UV-DAD spectrophotometer (Agilent Technologies, Santa Clara, CA, USA) operating under the control of Chemstation software release B.04-02. The data acquisition parameters were set to deliver a spectral resolution of 1 nm over the 190-1100 nm range [26].

Determination of the average hydrodynamic diameter and polydispersity index

The harvested nanoparticulate dispersions were profiled for their mean hydrodynamic diameter (effective particle size) and polydispersity index (PDI) by dynamic light scattering (DLS), making use of a non-invasive backscatter arrangement at a detection angle of 173° deployed on a Zetasizer® Nano ZS 90 instrument (Malvern Instruments, Malvern, UK). A refractive index of 1.330 was adopted for the optical model. Before each measurement (each performed in triplicate), the specimens were diluted to the appropriate concentration at a 1:100 ratio [5, 24, 26].

Nanoparticle tracking analysis NTA

The absolute particle concentrations in the AuNS and AuNR suspensions were determined by nanoparticle tracking analysis (NTA) on a NanoSight NS300 system (NanoSight, Amesbury, UK). Immediately before the assay, each sample was diluted 1:100 with Milli-Q water [24].

Scanning transmission electron microscopy (STEM)

To characterize the structural morphology of AuNSs and AuNRs in their native liquid environment, the specimens were visualized by scanning transmission electron microscopy using an FEI Inspect F50 instrument. The sample preparation protocol entailed depositing a 20 μL aliquot of each nanoparticulate suspension onto a Formvar/Carbon-Coated Copper 300-mesh grid for 2 min. Afterward, the grid was washed twice with Milli-Q water, dedicating 1 min to each rinse, and the remaining moisture was wicked away by gentle blotting onto absorbent Whatman paper [24, 26].

Design of matrices for 3D printing

To create the polymeric matrices intended as resin feedstocks for vat photopolymerization 3D printing, the equilibrium solubility of the model pharmaceutical Niclosamide in ternary liquid blends was investigated. The constituent ratios for these combinations were generated using Design-Expert software, employing a mixed-centered design strategy. The ternary mixtures comprised varying amounts of a photocurable monomer (PEGDA 250), a miscibility-enhancing co-solvent (PEG 400), and water, in which water served as the carrier vehicle for the nanoparticulate systems **(Figure 2)**. Using systematic variation, a panel of 13 matrix compositions was constructed, and the drug's solubility was quantitatively assessed in each. Every solubility measurement was carried out in triplicate [24].

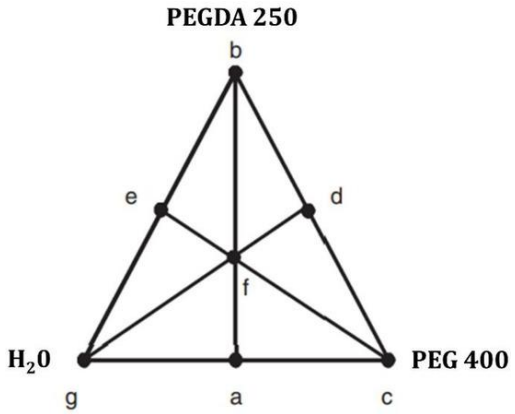

Figure 2. Mixture-simplex centroid design applied to the software Design Expert version 7.0.0.

Rheology

A rotational rheological assessment was performed using a cone–plate measuring system with a 50 mm-diameter upper element, installed on an Anton Paar Physica MCR 301 instrument capable of detecting torques down to 10^{-5} mNm. To extract flow behavior information across a broad shear rate window, the experimental protocol swept from 0.001 to 1000 s^{-1} [24].

The 3D-printing process

Cylindrical geometries possessing dimensions of 3 × 5 mm were modeled within the Fusion360 software suite v.2.0 (Autodesk Inc., San Francisco, CA, USA), and the corresponding build files were subsequently generated using the Chitubox slicing platform (CTB SDK, Shenzhen, China). An initial layer exposure duration of 65 s was

programmed, with successive layers receiving 4 s of illumination each. The prescribed layer thickness was 0.05 mm, the lift travel was fixed at 6 mm, and both the ascent and retraction speeds were configured to 180 mm/min. The physical constructs were fabricated on an Anycubic Photon S printer (Anycubic, Shenzhen, China); directly after completion, the green parts were cleansed with Milli-Q water and subjected to a 1 min post-exposure cure under 405 nm radiation inside an Anycubic Wash and Cure apparatus (Anycubic, Shenzhen, China) [19, 24].

Morphological analysis

The printed specimens were mounted on a pre-calibrated glass slide and visually inspected under an optical microscope (OLYMPUS Model BX-51, OLYMPUS, Tokyo, Japan) at 10× magnification [24].

Fourier-transform infrared evaluations

Attenuated total reflectance Fourier-transform infrared spectra (FTIR-ATR) of the liquid precursor mixtures and the corresponding solid printed materials were captured using an Agilent Technologies Cary 630 spectrophotometer. Spectra were accumulated over the wavenumber range of 4000 to 400 cm^{-1} with a spectral resolution of 1 cm^{-1}. The resulting datasets were managed and interpreted using the OMNIC® software environment (Thermo Fisher Scientific, St. Bend, OR, USA). Every spectral acquisition was performed in triplicate [24, 26].

Weight uniformity

In compliance with the specifications detailed in the United States Pharmacopeia (USP, 2007), the consistency of mass among the manufactured forms was evaluated. The procedure required weighing 10 identically sized printlets, calculating their mean mass, and verifying that no more than 2 individual values deviated from this average by more than 5%. Ten replicates from each matrix category were weighed individually on an analytical balance to determine the mass of each printlet. All weighings were conducted with the print held within a 1.5 mL Eppendorf tube. The balance was zeroed against an empty Eppendorf tube matched to the printed object before each measurement, ensuring that only the net mass of the printed object itself was captured [19, 24].

Scanning electron microscopy

The surface features and internal microstructure of the printlets were examined via scanning electron microscopy (SEM) on an FEI Inspect 50 system (USA) operated at accelerating voltages ranging from 3 to 20 kV, and micrographs were recorded at magnifications spanning 500× to 14,000×. To render the samples conductive, they were sputter-coated with a thin gold film before being introduced into the microscope chamber [24, 26].

Evaluation of the photothermal effect

A 532 nm laser module (LDCU5/9020, Power Technology, Alexander, AR, USA) and a 1064 nm laser module (IQ1A350, Laseray Inc., Cleveland, OH, USA) were each used to illuminate the AuNSs-loaded and AuNRs-loaded constructs, respectively, inside a fully enclosed dark box, to quantify the photothermal conversion arising from the nanoparticulates embedded within the printed matrices. For both sources, the radiant power was fixed at 350 mW. Thermal snapshots were collected by means of a FLIR E8xt thermal imaging camera (FLIR Systems Inc., Washington, DC, USA). Printed objects containing gold nanoparticles, together with nanoparticle-free control prints, were each immersed in phosphate-buffered saline (PBS) held in 1.5 mL Eppendorf tubes. The assemblies were subsequently exposed to laser light for 5 min, during which the temporal temperature variation was monitored to determine the photothermal contribution of the nanoparticulates residing within the 3D-printed structures [26].

Differential scanning calorimetry

Differential scanning calorimetry (DSC) analyses were performed to probe the thermal behavior of the specimens, with approximately 5 mg of sample used per analysis. The test materials were weighed and placed in perforated aluminum sample pans. DSC scans were recorded on a Discovery DSC 25P instrument (TA Instruments, New Castle, DE, USA) under a constant flow of nitrogen purge gas at 50 mL/min, with a heating rate of 5 °C/min and a temperature range from 25 °C to 250 °C. The calorimeter was calibrated against an indium reference standard (melting point = 156.6 °C; heat of fusion = 28.54 J/g) [5, 24].

Thermogravimetric analysis

Thermogravimetric measurements were performed using a Discovery HP TGA system (TA Instruments, New Castle, DE, USA). TGA mass-loss curves were generated by heating the samples from 25 to 350 °C under a dynamic nitrogen atmosphere at 50 mL/min, with a ramp rate of 5 °C/min. Subsequent data processing and analysis were conducted within the TRIOS software package (USA) [5, 24].

Evaluation of release without irradiation: phase solubility equilibrium

The printed constructs were immersed in PBS contained in 1.5 mL Eppendorf tubes and kept under constant orbital shaking at 250 rpm on a thermoshaker maintained at 37 °C. At specific sampling time intervals—namely 30 min, 60 min, 90 min, 120 min, and 4320 min (equal to 3 days)—a 1 mL portion of the supernatant was withdrawn and subjected to UV–Vis spectrophotometric analysis. After each measurement, the aspirated volume was returned to the original tube to maintain a constant cumulative drug-release environment. All release runs were conducted in triplicate [5, 19].

Assessment of drug release by laser irradiation

To examine drug liberation triggered by optical stimulation, the printed devices were positioned within 1.5 mL Eppendorf tubes and exposed to 15 min of uninterrupted laser irradiation originating from either a 532 nm laser (LDCU5/9020, Power Technology, Alexander, AR, USA) or a 1064 nm laser (IQ1A350, Laseray Inc., Cleveland, OH, USA). The concentration of the model drug accumulating in the release medium was monitored by recording UV–Vis absorbance at 333 nm every 1 min throughout the irradiation period. Each determination was repeated in triplicate [26].

Statistical analysis

All data points are expressed as the mean of the replicates ± the standard deviation (SD). Statistical evaluation and graphical representation were performed using GraphPad Prism version 7.0 (GraphPad Software, San Diego, CA, USA). Group comparisons were made using an analysis of variance (ANOVA). A probability value (p-value) of 0.05 or lower was regarded as indicative of a statistically meaningful difference [5, 24].

Results and Discussion

Synthesis process of gold nanoparticles with different morphologies

In the earliest stage of our experimental work, two separate nanoparticulate systems exhibiting non-overlapping plasmonic features were prepared. AuNSs and AuNRs were fabricated as a foundational proof of concept. **Figure 3** depicts the isolated plasmon band for AuNSs positioned at 532 nm and the pair of characteristic plasmon signatures for AuNRs: the primary longitudinal band situated at 1064 nm and a secondary, weaker band at 530 nm arising from the transverse plasmon mode [16, 25, 26].

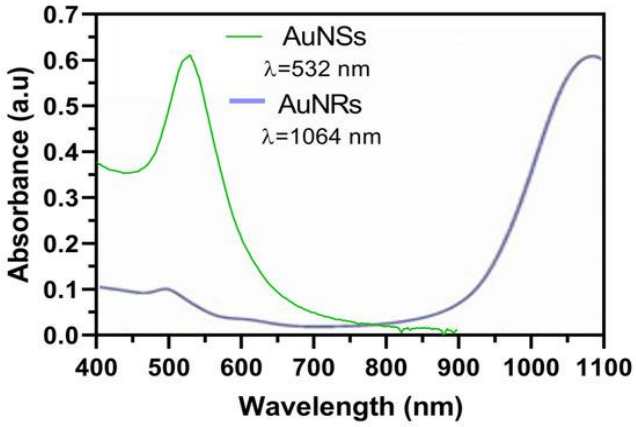

Figure 3. Plasmon resonance peaks of synthesized AuNSs and AuNRs determined by UV–Vis spectrophotometry.

Table 1 provides an extensive summary of the nanoparticulate systems' physicochemical profiling by reporting Zeta potential and hydrodynamic size measurements. This characterization extracts fundamental indicators of colloidal robustness, with Zeta potential magnitudes near ±30 mV generally indicative of a stable dispersion. Readings of this magnitude indicate the presence of a sufficiently strong electrostatic repulsive force, thereby diminishing the likelihood of particle clustering and the resultant breakdown of the colloidal state [16, 26]. Moreover, the determination of the hydrodynamic diameter supplies an estimate of the overall particle dimensions in solution. Caution must be exercised, however, as these values can be modulated by the intrinsic shape anisotropy of each nanosystem and by the measurement technique itself, which is predicated upon the observation of Brownian diffusion within the particulate suspension.

Table 1. Characterization of AuNSs and AuNRs by Zeta potential and hydrodynamic diameter.

Nanosystem	Zeta potential (mV)	Hydrodynamic diameter (nm)	Transverse hydrodynamic size (nm)	Longitudinal hydrodynamic size (nm)	PDI
AuNSs	−48 ± 2.8	27 ± 1.2	—	—	0.24
AuNRs	32 ± 0.3	—	4 ± 0.5	60 ± 16	0.47

The determinations were performed in triplicate.

Regarding the AuNSs, the measured Zeta potential was −48 ± 3 mV, indicating excellent colloidal stability. This negative surface potential arises from the sodium citrate layer used as the capping and reducing agent during AuNS synthesis [16]. Concurrently, the hydrodynamic diameter was determined to be 27 ± 1.2 nm. It is pertinent to note that whereas the size anticipated from the preparative recipe was roughly 10 nm, hydrodynamic measurements inherently capture the surrounding hydration layer, thereby justifying a moderate inflation of the reported value.

For the AuNRs, the Zeta potential was 32 ± 0.3 mV, indicating the sought-after colloidal stability. This positive surface charge originates from the CTAB surfactant used as a structure-directing stabilizer during synthesis, whose molecular framework incorporates a positively charged quaternary ammonium headgroup [26]. Furthermore, the transverse hydrodynamic dimension was determined to be 10 ± 1 nm, and the longitudinal hydrodynamic dimension 60 ± 16 nm. It is nevertheless critical to acknowledge that, owing to the non-spherical character of these structures, the values obtained by dynamic light scattering may be subject to artifacts, and the definitive measurements taken forward for subsequent interpretation were those acquired via electron microscopy.

Characterization of nanosystems by NTA and STEM

Presented in **Figure 4a** is an evaluation of the mean size of the nanosphere population, which was determined to be around 35 nm using NTA. Alongside this, the figure shows a broader particle dispersion spanning 0–100 nm, with an average nanoparticle titer of 176 pM. Turning to **Figure 4b**, the structural morphology of the nanospheres as visualized by STEM is displayed, from which an average diameter of roughly 16 nm was deduced.

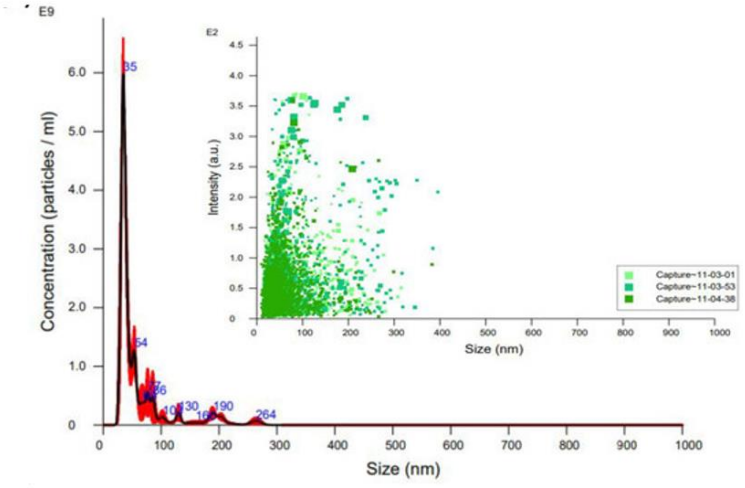

a)

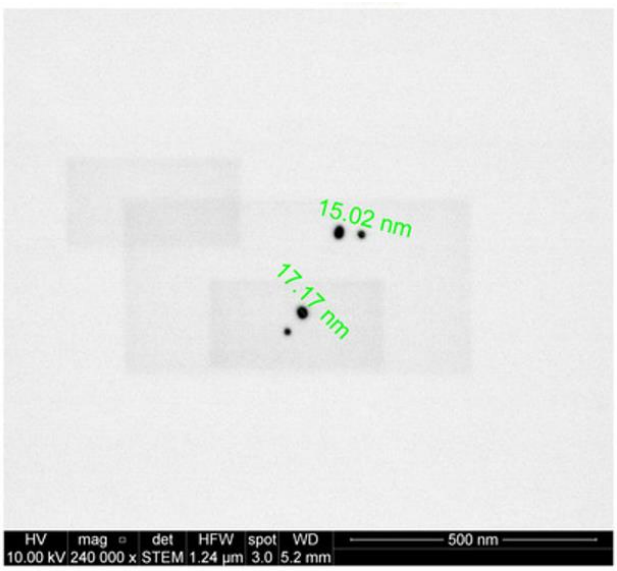

b)

Figure 4. Characterization of AuNSs by (a) NTA (different captures of the same sample obtained are represented in different green tones) and (b) STEM.

A marked disparity is evident in the AuNS size estimates, with NTA yielding substantially larger values than STEM. This divergence plausibly originates from the potential formation of nanoparticulate clusters within the liquid dispersion, entities that the NTA instrument may register as single events [13]. Electron microscopy, by virtue of its ability to image discrete particles directly, provides measurements that override this limitation. The STEM-derived figures are regarded as the definitive reference standard. Consequently, it may be stated with a high degree of assurance that the synthetic protocol yielded nanospheres conforming to the intended size range and spherical morphology.

Depicted in **Figure 5a** is the mean size for AuNRs, which was recorded at 138 nm, paired with a comparatively broad size distribution extending from 100 to 200 nm. The mean nanoparticle titer post-synthesis stood at 26.6 pM. Following this**, Figure 5b** reveals the morphological characteristics of the AuNR population as captured by STEM, yielding an estimated average length of 71 nm. Notably, the STEM-derived dimensions remain smaller than the values returned by NTA. Such a discrepancy can again be attributed to the inherent geometric anisotropy of AuNRs [25, 26].

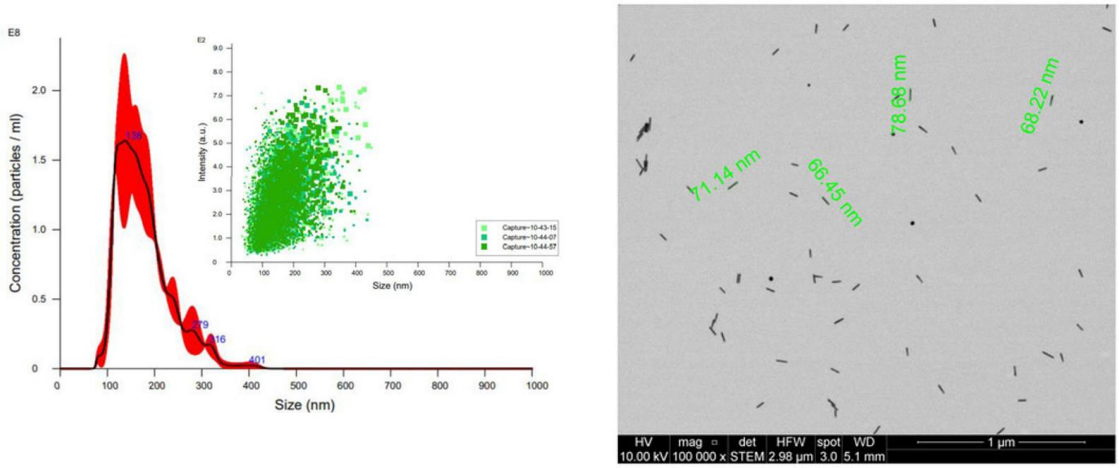

a) b)

Figure 5. Characterization of AuNRs by (a) NTA (different captures of the same sample obtained are represented in different green tones) and (b) STEM.

Evaluation of the solubility of niclosamide in ternary mixtures

Leveraging a mixed-centered design strategy delivered through the Design Expert software environment, ternary formulations blending PEGDA 250, PEG 400, and water (the latter acting as the suspending vehicle for the nanoparticulate components) were successfully devised, as itemized in **Table 2**. This methodical framework enabled a detailed investigation of the dissolution profile of the model drug, Niclosamide, across the prospective matrix compositions.

Table 2. The diverse array of component ratios involving PEGDA 250, PEG 400, and water of the 13 matrices under examination. The right-hand side of the table provides the 17 corresponding solubilities of Niclosamide in micrograms per milliliter (μg/mL) within each of these matrices. The selected matrices are highlighted in bold.

Run	A: PEGDA 250	B: PEG 400	C: H_20	NICLO SOLUBILITY (ug/mL)
1	0.2	0.35	0.45	54.4
2	**0.2**	**0.7**	**0.1**	**11,778.6**
3	0.316667	0.466667	0.216667	4773.3
4	0.55	0	0.45	218.4
5	**0.55**	**0.35**	**0.1**	**5370.7**
6	**0.9**	**0**	**0.1**	**4069.5**
7	0.666667	0.116667	0.216667	57.6
8	0.2	0	0.8	142.7
9	0.2	0	0.8	13.1
10	0.9	0	0.1	3974.7
11	0.433333	0.233333	0.333333	56.1
12	0.316667	0.116667	0.566667	16.0
13	0.2	0.7	0.1	13,395.8

The photocurable oligomer PEGDA plays an essential regulatory role by modulating the density of covalent crosslinks formed between monomeric repeat units during light-driven solidification of the liquid resin. The resultant crosslink density profoundly influences both the viscoelastic response and the ultimate fidelity of the printing process [20]. It is additionally worth emphasizing that a minimum aqueous fraction of 10% was maintained across all formulations, without exception, as the water phase served as the delivery medium for integrating the nanoparticulate suspensions.

Throughout the assessment of the 13 candidate blends, a response surface plot was constructed, as portrayed in **Figure 6**. An unmistakable tendency was observed: mixtures with a higher proportion of PEG 400 displayed progressively higher Niclosamide solubility, with PEGDA showing a weaker solubilizing effect. The preferential dissolution of NICLO in PEG 400 as opposed to PEGDA 250 can be rationalized through the molecular and physicochemical divergence between these two carriers. On one level, PEG 400 is an unbranched polyether with substantial backbone flexibility and an abundance of hydrophilic functional groups, namely terminal hydroxyls and backbone ether oxygens (–OH and –O–). This structural motif fosters extensive hydrogen-bonding networks with both water molecules and polar drug species, thereby augmenting solvation capacity. Conversely, PEGDA 250, while built around a central polyethylene glycol segment, is derivatized at both chain ends with acrylate moieties that are intrinsically more reactive yet less water-compatible than the terminal hydroxyls found in neat PEG. The incorporation of acrylate caps restricts backbone mobility and is likely to reduce the extent of hydrogen-bond-mediated contacts available for interaction with the solute. In addition, PEG 400 possesses a considerably lower bulk viscosity than PEGDA 250. The increased viscosity of PEGDA 250 could suppress the diffusive mobility of dissolved drug species throughout the fluid phase, thereby impeding dissolution. In summation, PEG 400 offers superior conformational adaptability, greater hydrophilicity, and a less sterically hindered molecular architecture relative to PEGDA 250, all of which may enhance the solubility of a drug in PEG 400 due to its enhanced aptitude for intimate molecular-level engagement with dissolved species [20].

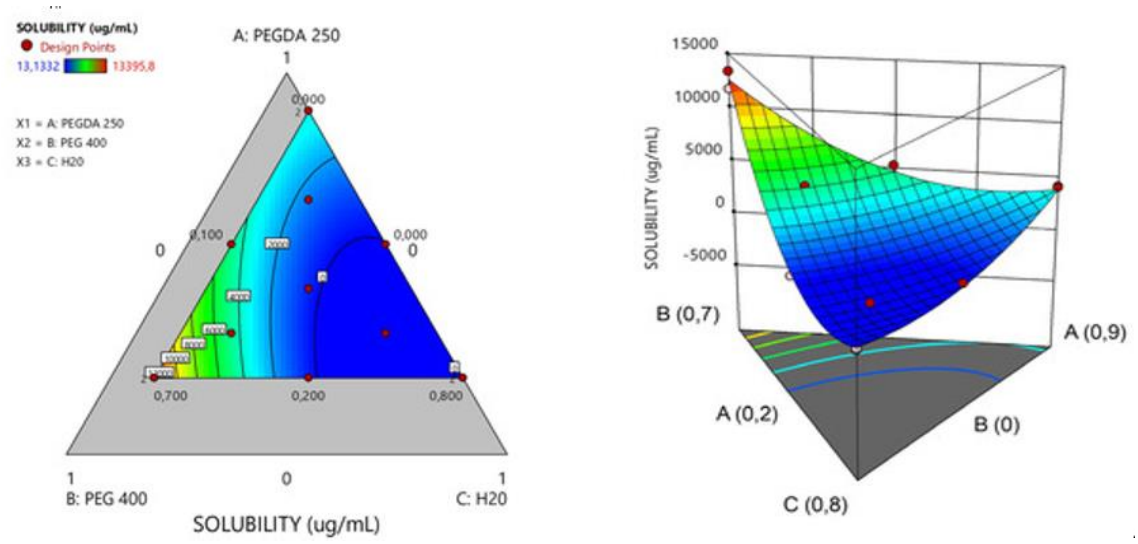

a) b)

Figure 6. Response surface plots of ternary PEGDA/PEG400/water mixtures—evaluation of the solubility of the model drug Niclosamide at 25 °C.

To progress to the characterization phase, matrix compositions with the greatest ability to dissolve Niclosamide were prioritized to ensure maximal incorporation of the therapeutic payload. It bears underscoring that the model drug demonstrated a predilection for the non-photocurable constituent, PEG 400. As such, compositions attaining the highest NICLO solubility readings while spanning a range of PEGDA-to-PEG 400 proportions were identified. More precisely, three formulations with distinct PEGDA loadings and diverging PEGDA/PEG 400 ratios—denoted as experimental runs 2, 5, and 6 (presented in bold typeface)—were selected for onward assessment of their suitability for the printing process.

Table 3 summarizes the compositional breakdown of PEGDA, PEG 400, and water within these chosen matrices, paired with the Niclosamide drug loading expressed in µg/mL for each. Matrix 6 registered the highest PEGDA 250 fraction at 90%, with Matrix 5 and Matrix 2 trailing at 55% and 20%, respectively. Every chosen matrix uniformly contained 10% water (within which the nanosystems were dispersed), and the remaining volume was made up by the co-solvent PEG 400. The working concentrations of AuNSs and AuNRs employed were set at 17.6 pM and 2.66 pM, respectively, in a total batch volume of 50 mL per matrix. The adoption of lower AuNR loadings reflects their recognized greater photothermal transduction performance relative to AuNSs.

Table 3. Selected formulation composition and drug loading (DL%).

Matrix	PEGDA 250 (%)	PEG 400 (%)	H_2O (%)	NICLO (µg/mL)	DL%	AuNSs/AuNRs [pM]
2	0.2	0.7	0.1	11,700.0	1.06	17.6/2.66
5	0.55	0.35	0.1	5300.0	0.48	
6	0.9	0	0.1	4000.0	0.36	

Rheology

To further probe the matrices' behavior, a rotational rheological evaluation was performed to clarify the viscoelastic characteristics of the materials in their pre-photopolymerization state.

From a rheological perspective, SLA resins operate predominantly in a Couette flow regime; therefore, rotational rheometric testing is the most representative analytical methodology [27]. One important element to bear in mind is that the constructs are manufactured in an inverted arrangement, meaning a sufficiently low shear viscosity is permanently required to allow the formulation to spread across the traversing build stage. At the same time, however, once a portion of the structure has been solidified, sound mechanical properties and the capacity to sustain minor stresses become essential to keep the part adhered to the build plate and to bear the successively added layers.

In SLA-based printing, both the working viscosity and the encountered shear rates are relatively small. Conventionally, the resin viscosity should remain below 5 Pa·s at a shear rate of 30 s^{-1}, a criterion that ensures unimpeded resin flow and the reliable formation of a fresh liquid layer poised for photopolymerization [28]. The

specific printer hardware and the configured print settings will ultimately dictate this limiting value. As portrayed in **Figure 7**, PEGDA 250 demonstrated the greatest shear-thinning behavior, reaching the lowest viscosity under increasing shear, whereas PEG 400, at the opposite extreme, preserved the highest viscosity readings. This rheological signature may be explained by the comparatively higher molecular mass of PEG 400, which promotes greater molecular structuring. Matrix 6, in turn, displayed a flow response closely paralleling that of neat PEGDA 250, consistent with PEGDA 250 being the major constituent in this blend. Within this system, the impact of AuNSs and AuNRs was specifically scrutinized, and it was noted that, within the low-shear region, AuNR-loaded systems exhibited viscosities more closely aligned with those of pure PEGDA 250. This observation may be traced to the residual CTAB from the AuNR synthesis step. The surfactant character of this molecule likely favors better miscibility between the aqueous phase and the photopolymer, nudging the viscoelastic response of the entire formulation toward that of the predominant PEGDA 250 component. Matrices 5 and 2, by contrast, registered markedly higher viscosities, following a monotonic trend with the incremental addition of PEG 400; Matrix 2, incorporating 70% PEG 400, proved to be the most viscous of the set.

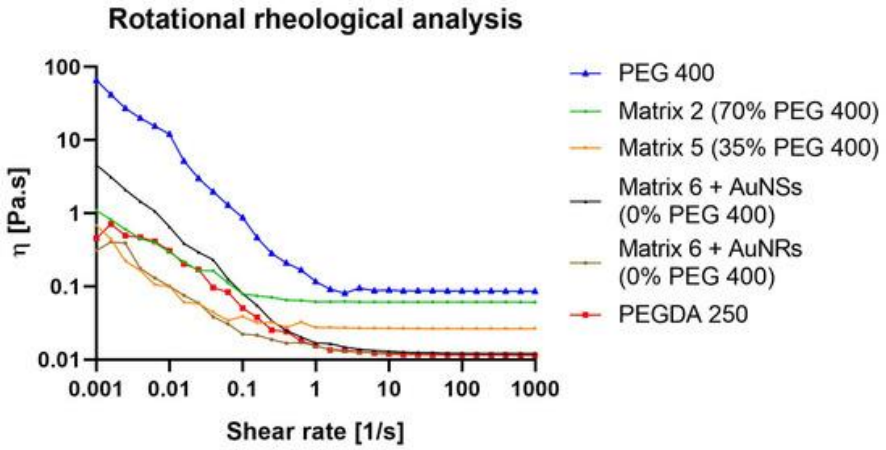

Figure 7. Rotational rheological analysis of PEGDA 250, PEG 400, and 3D-printing matrices 2, 5, and 6 (with AuNSs or AuNRs).

3D printing

The compositions designated as runs 2, 5, and 6 were selected for fabrication, all of which relied on PEGDA 250 as the scaffold-forming photopolymer. The target shape assigned for the print job was a cylindrical geometry with dimensions of 3 × 5 mm. This model was crafted within the Fusion 360 CAD platform and readied for output by generating the slice plan in Chitubox 64, resulting in a build stack of 100 layers. The finished digital instruction file was subsequently uploaded to an Anycubic Photon S printer (Anycubic Technology Co., Shenzhen, China), initiating the print sequence, which concluded after roughly 20 min. After the print cycle, the fabricated pieces were solvent-rinsed and post-cured in an AnyCubic Wash and Cure Station for 1 min. The as-manufactured parts were then subjected to a multi-step characterization routine that included optical microscopy, determination of weight uniformity, and SEM-based morphological examination.

Images obtained by optical microscopy

Matrices 2, 5, and 6 were successfully formulated into printable resins, yielding the solidified artifacts shown in **Figure 8a** under an optical microscope. The solid bodies generated from Matrices 2 and 5 deviated noticeably from the intended dimensional targets. Nevertheless, such departures provided valuable feedback for a preliminary mapping of the operational envelope within which the compositional ratios would permit a successful print outcome. On the other hand, Matrix 6 exhibited markedly reduced optical transparency, suggesting a greater extent of covalent network formation (as evidenced) **(Figure 8c).** This observed outcome can be linked to the increasingly dominant fraction of PEGDA 250 within the formulation.

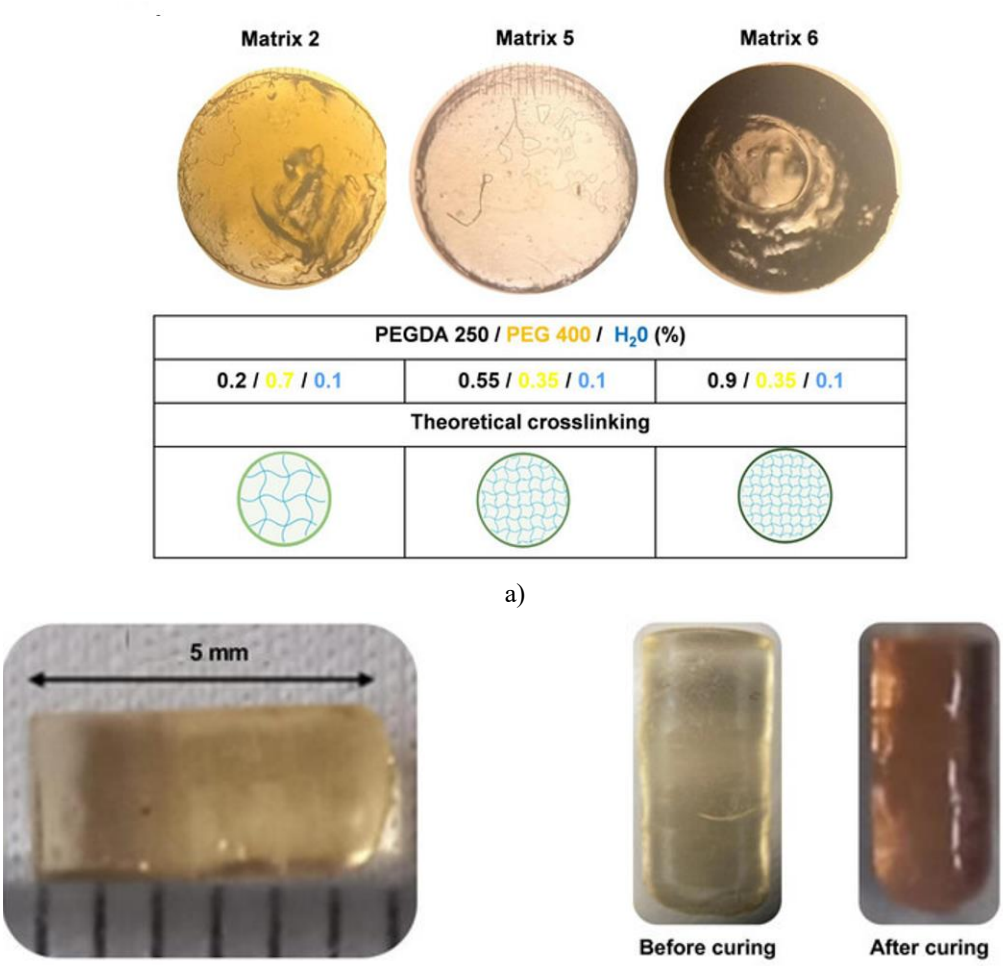

Figure 8. (a) Microphotographs of prints acquired through optical microscopy, (b) Images of the device resulting from Matrix 6 with PEGDA 250, and (c) Device before and after the curing process.

The degree of match between the digitally prescribed design and the physical prints varied by printing medium. Across all the trials, the cross-sectional dimension of the printed parts remained statistically reproducible, registering an average width of 2.87 ± 0.1 mm. However, the constructs fashioned with Matrices 2 and 5 did not attain the expected 5 mm length, instead producing noticeably foreshortened parts measuring approximately 2 mm. **Figure 8b** depicts a representative print produced with Matrix 6. For objects fabricated from this particular composition, the dimensional correspondence with the original CAD file was remarkably precise. Based on these results, it may be inferred that the PEGDA 250 fraction within the resin is an essential factor for achieving favorable printability attributes.

In addition, the printed items exhibited a distinct color transition upon post-curing, as shown in **Figure 8c**. This chromatic alteration may be assigned to the higher radiant flux of the curing lamp, which drove a greater degree of crosslinking and consequently reorganized the material's internal architecture. Two principal mechanisms could account for this effect. First, during the curing phase, PEGDA polymerization approached completion, as evidenced by a color change [29]. Second, this phenomenon, in conjunction with the incorporation of gold nanoparticles, altered the material's visual appearance due to the altered surroundings in which the particles were suspended. It is striking that this color change was universally noted across all matrix compositions. From this, it can be inferred that the effect is more closely associated with the gold nanoparticle component, given that the extent of photopolymerization was presumably different across the matrices due to the varying PEGDA/PEG ratios. Analogous observations have been reported in the literature. In a pertinent study, it was reported that increasing the concentration of a gold chloride precursor shifted the absorption maximum of the resultant materials

from roughly 540 nm to approximately 560 nm, resulting in a visible color shift in a hydrogel from a lighter tone to a deeper, bluish-purple shade [30].

FTIR

To gauge photopolymerization conversion and explore potential intermolecular associations among formulation constituents, FTIR spectra were collected for the matrices in two distinct states: the initial liquid state (non-photopolymerized precursors) and the final solid state (3D-printed products). Within the spectral interpretation, the hallmark vibrational bands of PEGDA were assigned to the C–O stretching modes of the ester functionalities, which appear at 1270 cm^{-1}, 1190 cm^{-1}, and 985 cm^{-1} [31, 32]. After the curing step, the FTIR signatures of the matrices underwent pronounced transformations as a direct consequence of irradiation and the ensuing crosslinking copolymerization. More precisely, under UV exposure, the photoinitiator underwent photolysis, generating propagating radical species that could open carbon–carbon double bonds along the monomer backbone, thereby facilitating network formation. The advancement of the photopolymerization was verified by tracking the attenuation of the olefinic absorption signals positioned at 1636, 1618, 1410, and 810 cm^{-1} [33, 34]. As depicted in **Figure 9**, by the conclusion of the UV curing stage, the signals attributable to unsaturated bonds in the pure PEGDA specimen had been drastically diminished, indicating their continuous consumption by the active radical centers, which in turn contributed to the solidification process and enhanced the crosslink density. The complete disappearance of infrared absorptions assignable to unreacted C=C bonds (with emphasis on the characteristic band at 810 cm^{-1}) from the spectra of the 3D-printed materials signified that the curing of the resin formulations had proceeded to a satisfactory degree. This observation is particularly relevant to biomedical applications, as the extent of double-bond conversion is closely tied to the material's ultimate biocompatibility. Any lingering unreacted radical groups can serve as potential irritants, causing damage to adjacent soft tissues [35].

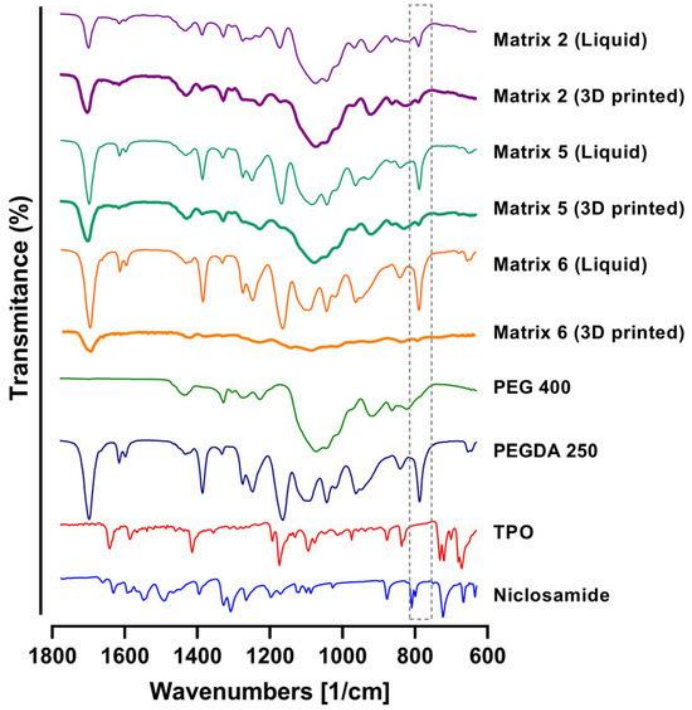

Figure 9. FTIR spectra of PEGDA, PEG 400, TPO, Niclosamide, and 3D-printing Matrices 2, 5, and 6. Note: the gray dotted box is to focus on the decrease in the signal of the C=C bonds in the 3D printed matrices.

Weight uniformity

The mass uniformity of the printed articles was investigated to extract a quantitative descriptor of process quality. This evaluation enabled an appraisal of both the fidelity of the printing operation and the intrinsic printability of the resin matrices [24]. Beyond this, the drug payload of each print was back-calculated from its measured mass and the known starting concentration of Niclosamide solubilized within the matrix.

Ten replicate prints from each formulation were weighed on an analytical microbalance for the uniformity study, after which the arithmetic mean weight and the corresponding standard deviation were derived. **Table 4** reports

the mean weight values assembled from 10 replicates across all the printed matrix categories. For Matrix 2, the mean weight was 1.97 mg with a standard deviation of 0.34. These figures suggested that the printing outcomes for this particular matrix were unfavorable in terms of quality. Nonetheless, the standard deviation across the ten specimens remained below the 0.4 threshold, indicating that although the prints fell short of the anticipated dimensional specification, the printed devices exhibited acceptable reproducibility among themselves. Put differently, the print process was inaccurate to the target but precise. Furthermore, it is pertinent to underscore that the back-calculated Niclosamide content, while on the order of 0.019, is likely unreliable due to the printing anomalies observed.

Table 4. Weight distribution, niclosamide content per device, drug loading (DL%), and entrapment efficiency (EE%) in printed objects using Matrices 2, 5, and 6.

Matrix	Average weight (mg)	Standard deviation	Amount of niclosamide per device (mg)	DL%	EE%
2	1.97	0.34	0.02	0.96	90.67
5	2.05	0.29	0.01	0.45	95.02
6	14.97	0.11	0.05	0.33	91.85

In a manner comparable to Matrix 2, the batches produced from Matrix 5 exhibited flaws in which a subset of devices remained adhered to the base of the resin container rather than being anchored to the build plate, thereby displaying evident inconsistencies **(Figure 10a).**

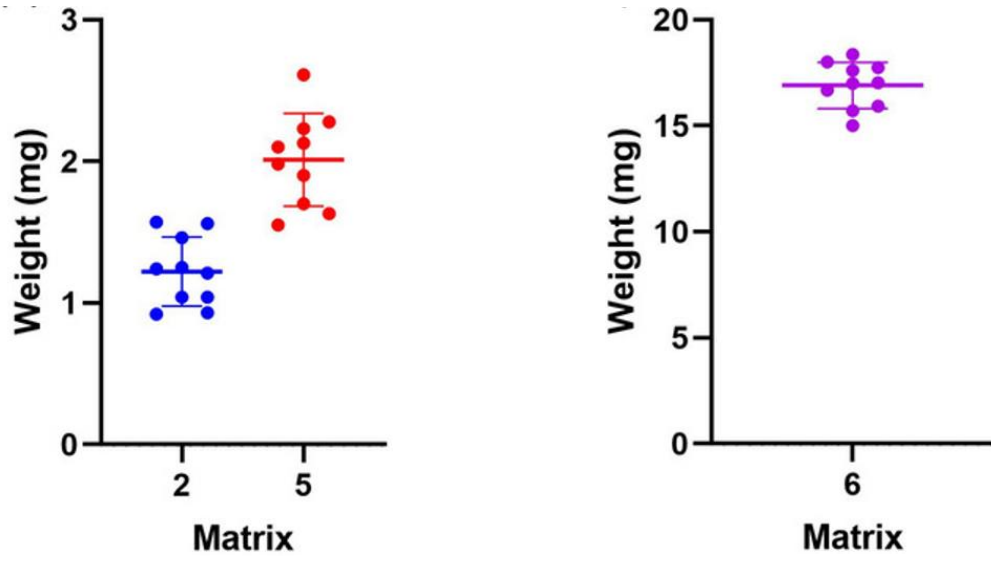

a) b)

Figure 10. Weight uniformity of 3D-printed devices employing different photopolymerizable matrices: (a) Distribution of weight uniformity for matrix 2 in blue and matrix 5 in red, and (b) Distribution of weight uniformity for matrix 6 in violet.

In marked contrast, for Matrix 6, the mean weight per part reached 14.97 mg, paired with a considerably narrower standard deviation of merely 0.1 **(Figure 10b)**. Only an occasional device suffered from the adhesion failure noted above, with the great majority remaining properly secured to the build platform. From the weight of this evidence, it can be inferred that Matrix 6, formulated with the highest PEGDA 250 proportion, demonstrated the greatest potential for reliable fabrication via VAT photopolymerization. Based on the cumulative results summarized above, Matrix 6 alone was advanced to the next phase of experimental testing.

SEM

SEM was used to visualize the printed parts generated from Matrix 6 containing either AuNSs or AuNRs to examine their surface architecture. As illustrated in **Figure 11a**, the fabricated structures exhibited a morphology that mirrored the input digital file, displaying a smooth exterior surface free of perceptible boundaries between consecutive printing layers. **Figure 11b** shows magnified surface detail for prints loaded with AuNSs (left) and

AuNRs (right). In neither case were discrete drug crystals observed, nor did the nanoparticulate additives appear prominently at the outermost plane.

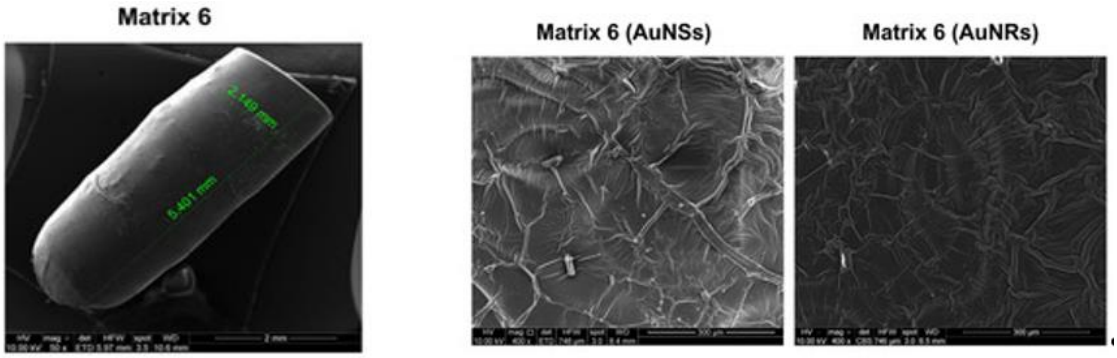

Figure 11. Characterization of prints obtained with Matrix 6 loaded with AuNSs and AuNRs using SEM.

Energy-dispersive X-ray Spectroscopy (EDX) was employed to perform elemental microanalysis of the printed construct produced from Matrix 6, composed of PEGDA 250 and AuNSs; the results are shown in **Figure 12**, along with the corresponding elemental percentage composition [19, 24]. Carbon and oxygen emerged as the overwhelmingly dominant elements within the solid framework. This finding aligns with the organic molecular constituents forming the backbone of the polymer network, most notably PEGDA 250 and PEG 400. The detection of chlorine was definitively linked to Niclosamide, thereby corroborating the successful entrapment of the model drug within the device. Phosphorus signals were also detected, plausibly originating from the TPO photoinitiator species, whose molecular structure incorporates this heteroatom.

Element	Composition (%)
Carbon	50.7
Oxygen	48.2
Phosphorus	0.48
Chlorine	0.44
Total	100

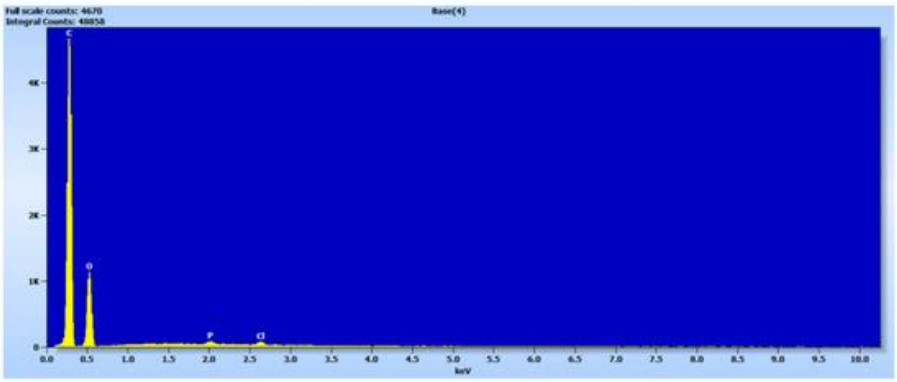

Figure 12. Elemental analysis of the solid device obtained using Matrix 6.

In accordance with the accepted photopolymerization mechanism, the TPO initiator undergoes photolytic cleavage, fragmenting into a benzoyl radical and a phosphorus-bearing acid radical, both of which subsequently initiate the chain-growth polymerization of PEGDA by adding across the available acrylate double bonds [34]. For this reason, future efforts should be directed toward establishing the precise chemical form in which the phosphorus resides, specifically whether it is present as part of a radical moiety or as intact, unreacted TPO molecules.

It is noteworthy that the elemental mapping failed to register any detectable gold signal. This finding suggests that the nanoparticle loadings utilized fell beneath the instrumental detection limit, or that the nanoparticulate fillers

were more uniformly dispersed within the interior volume of the prints, residing deeper beneath the surface rather than concentrating at the outer skin.

Photothermal effect of the prints

To confirm that the nanoparticles had been successfully embedded within the fabricated constructs, their light-to-heat conversion capacity was tested by directing a 532 nm laser onto AuNSs-loaded prints and a 1064 nm laser onto AuNRs-loaded prints [26]. Control specimens manufactured without any nanoparticulate additives were tested under matching conditions, exhibiting only ~1 °C of thermal gain after 5 min of continuous exposure to either wavelength **(Figure 13)**. The AuNS-functionalized Matrix 6 print showed a temperature increase from a baseline of 25 °C to 29.9 °C after 5 min of 532 nm illumination. The device underwent a roughly 5 °C temperature jump upon irradiation, verifying that the nanoparticles were satisfactorily dispersed within the polymeric host and that their loading level was sufficient to elicit a detectable photothermal response. Equivalent confirmation was obtained for AuNRs-bearing systems, where a thermal swing from 21.2 °C to 45.5 °C was recorded over an identical 5 min irradiation window. Here, the magnitude of the temperature differential approached 24.3 °C over the same timespan, even though the AuNR concentration was tenfold lower. This pronounced disparity underscores the considerably greater photothermal conversion performance of AuNRs relative to their spherical counterparts [26].

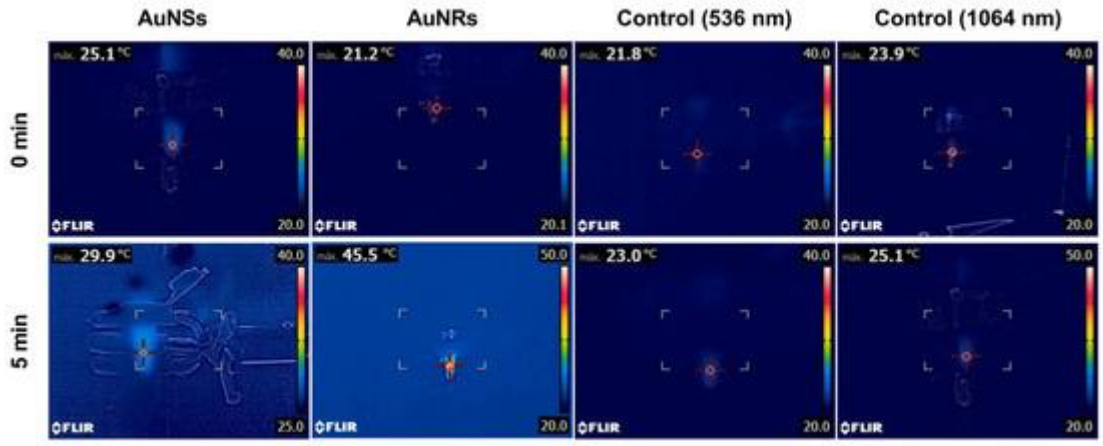

Figure 13. The photothermal effect of controls and the printed device from Matrix 6 with AuNSs or AuNRs after 5 min of irradiation with a 536 nm or 1064 nm laser, respectively.

DSC and TGA

Motivated by the validated photothermal behavior of the 3D-printed articles, the bulk thermal properties of the constituent materials were subsequently evaluated. **Figure 14a** depicts the calorimetric signatures obtained through DSC measurements. Niclosamide in its pure form exhibited a sharp melting endotherm at 233 °C, a temperature well above any thermal excursions observed during the laser irradiation experiments [24]. It was therefore reasonable to conclude that neither polymorphic transitions nor thermal decomposition of the drug would occur under the device's operational parameters. For the cured prints derived from all three matrix formulations, the characteristic melting peak of Niclosamide was conspicuously absent, suggesting that the photopolymerization-driven crosslinking event promoted Niclosamide's conversion to an amorphous state within the solidified network.

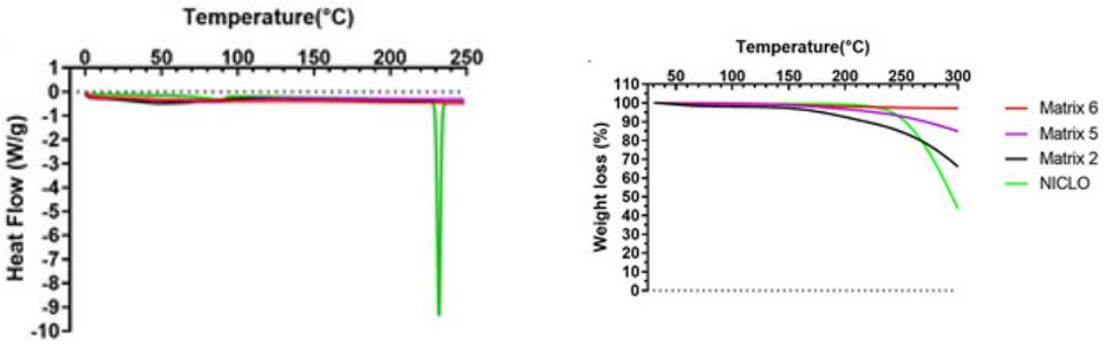

b) c)

Figure 14. DSC (a) and TGA and (b) analyses of Niclosamide and 3D-printed objects obtained using Matrices 2, 5, and 6.

Figure 14b sets out the thermogravimetric decomposition traces. As observed, Niclosamide underwent a steep mass decrease commencing after its melting point at 233 °C. In the case of the printed specimens produced from Matrices 2 and 5, no appreciable mass loss was detected at temperatures falling below 150 °C. Above this threshold, a gradual weight decline was observed, attributed principally to the volatilization of residual moisture and the progressive elimination of the PEG 400 fraction from the prints; this phenomenon was notably more pronounced in the Matrix 2-derived samples. The Matrix 6 specimens, by contrast, exhibited negligible mass fluctuations over the entire probed thermal range, up to 300 °C.

Drug release from the matrices without irradiation

The printed constructs were evaluated in dissolution experiments conducted with and without accompanying laser irradiation to assess the selectivity of the drug-release mechanism. Passive release trials were first conducted to identify which candidate formulation most effectively minimized drug escape in the absence of photonic stimulation, as shown in **Figure 15** [5]. In general, a modest burst efflux of the drug was observed during the initial 30 min of immersion, followed by a protracted plateau that remained steady for the full 4320 min (3-day) observation window. Although rigorous statistical comparison did not reveal significant differences among the matrices, the print that released the smallest cumulative quantity of Niclosamide was that fabricated from Matrix 6 (0.5 µg/mL, equating to approximately 1%), a finding in line with its most highly crosslinked architecture, attributable to the elevated PEGDA 250 fraction.

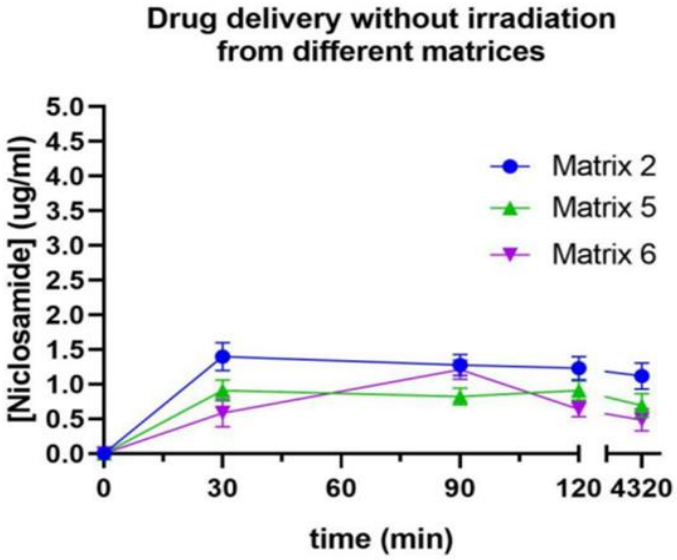

Figure 15. Release profile of Niclosamide without irradiation from Matrices 2, 5, and 6 measured by UV–Vis spectrophotometry.

Given its minimal passive drug leakage when not irradiated, Matrix 6 was selected as the carrier of choice for the next phase of triggered-release investigations. The integration of plasmonic nanostructures into this optimized matrix was expected to yield a discernible modulation in the release profile of the active species, whether manifested as an altered elution rate or a shift in the governing release mechanism. Thus, the compositional ratio that yielded the lowest background release under non-irradiated conditions was deliberately advanced, on the assumption that drug output would increase considerably once the device was challenged with the appropriate optical trigger.

Drug release from prints with AuNSs and AuNRs and the bilayer device under irradiation at different wavelengths
The time-dependent concentration of Niclosamide in the release medium was monitored after subjecting printed platforms—encompassing Matrix 6 formulations loaded solely with AuNSs, solely with AuNRs, and a bilayer construct merging both nanoparticulate populations in vertically distinct compartments—to laser light. For this experimental series, each printed device was submerged in 1.5 mL of PBS, and small-volume aliquots were withdrawn at 1 min increments throughout a 15 min uninterrupted irradiation period. UV analyzed the aspirated samples–Vis spectrophotometry, and the corresponding Niclosamide concentrations were back-calculated by reference to a predetermined standard curve.
Figure 16 outlines the Niclosamide elution trajectory from the AuNSs-containing Matrix 6 print under 532 nm laser excitation. A swift upsurge in Niclosamide concentration was observed over the initial 10 min of light application (attaining 0.9 μg/mL, reflecting a release velocity of 0.09 μg/min), whereupon the liberation tempo declined through to the terminal 15 min time point (reaching 1 μg/mL, a release velocity of 0.02 μg/min), ultimately yielding a cumulative 2% Niclosamide discharge following 15 min of irradiation.

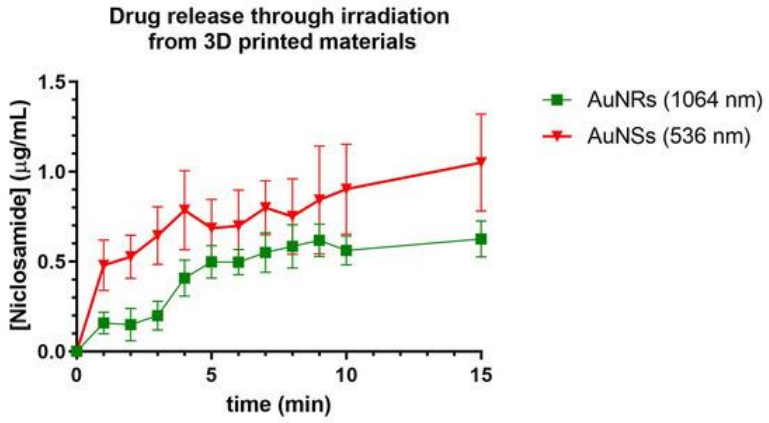

Figure 16. Release of Niclosamide from the print of Matrix 6 of AuNSs after irradiation with the 536 nm laser. Niclosamide was released from the print of Matrix 6 with AuNRs following irradiation with the 1064 nm laser—data obtained from the UV–Vis spectrophotometer.

Compared with non-irradiated controls, the light-exposed AuNS-equipped Matrix 6 showed the same percentage of Niclosamide liberation in half the time (15 min). This observation points to the platform's genuine photoresponsiveness. It suggests that the AuNSs distributed within the print effectively convert incident photons into localized thermal gradients, thereby accelerating the escape kinetics of the co-formulated drug [26].
The elution of Niclosamide was likewise assessed from 3D-printed entities composed of AuNRs-doped Matrix 6 following exposure to a 1064 nm laser. The resultant release traces largely paralleled those acquired from the AuNSs-based systems, typified by a sustained efflux phase persisting for up to 10 min (peaking at 0.5 μg/mL, with a release rate of 0.05 μg/min), after which the liberation speed dwindled toward the 15 min mark (0.55 μg/mL, release rate falling to 0.01 μg/min). These data similarly confirm that the AuNRs-bearing construct responds to the optical cue by liberating Niclosamide from the polymeric reservoir.
Notably, the AuNRs-loaded devices achieved markedly higher temperatures than the AuNSs systems, yet this thermal advantage did not translate into a commensurately greater drug output; in fact, the release rate proved comparatively diminished. This seeming contradiction can be plausibly reconciled by considering the substantially lower nanoparticle titer in the AuNRs prints. This experimental variable carries mechanistic significance, as it tentatively suggests that drug liberation may be governed by the photothermally driven

formation of nanoscopic channels within the polymer continuum, which act as portals enabling the ingress of the surrounding dissolution medium into the interior of the print, thereby facilitating drug solubilization and subsequent outward flux. **Figure 17** shows the Niclosamide release profile of the bilayer construct under sequential irradiation with 532 nm and 1064 nm lasers. The optical exposure protocol was identical to that employed for the single-nanoparticle Matrix 6 prints. Thereafter, illumination with the 1064 nm source was commenced, resulting in a steady increase in Niclosamide concentration that eventually plateaued at the 30 min sampling point. From the assembled kinetic data, it can be deduced that the bilayer device can differentially respond to distinct irradiation wavelengths, thereby releasing the model therapeutic, Niclosamide, in a regulated manner.

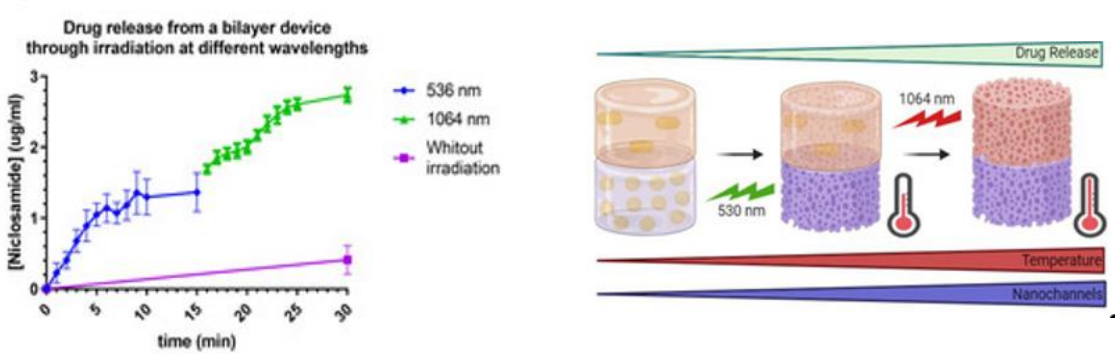

a) b)

Figure 17. (a) Release of Niclosamide from the bilayer device after laser irradiation with 532 nm and 1064 nm. Data were obtained through measurement with the UV–Vis spectrophotometer, and (b) Schematic representation of the designed photothermal-controlled drug release bilayer device.

As is evident, the release during the first 15 min phase (under 532 nm light) yielded a kinetic curve strikingly reminiscent of that recorded for the standalone AuNSs print **(Figure 16),** albeit with slightly higher absolute values, reaching 1.2 µg/mL at 15 min. This modest elevation of around 0.2 µg/mL can be reasonably attributed to a minor contribution of drug leaching from the adjacent AuNRs compartment, potentially triggered either by the secondary transverse plasmon resonance of the nanorods or by passive thermal conduction across the interface between the two superimposed layers. In marked contrast, the release observed over the subsequent 15 min interval was substantially amplified, reaching 2.8 µg/mL at the 30 min terminus. This enhanced liberation can be rationalized by the cumulative heating effects wrought by the prolonged aggregate irradiation duration, in tandem with a likely expansion in both the density and the dimensions of the nanochannels generated within the material architecture, leading to augmented swelling of the construct, which in turn could promote a greater extent of drug mobilization from both constituent layers, as conceptually illustrated in **Figure 17b**.

Conclusion

The utility of 3D printing in photothermal therapy holds considerable translational promise. This fabrication approach enables the generation of highly individualized medical platforms tailored to each patient's specific requirements, a factor of particular relevance in oncological care, where inter-tumoral heterogeneity is pronounced. Beyond personalization, 3D printing enables the architecture of complex, microscale geometries that can augment the therapeutic efficacy of photothermal interventions. It further enables the construction of nanoparticulate entities and sensing elements for the programmed liberation of drugs and the real-time tracking of tissue-level responses throughout treatment. Collectively, these advances possess the potential to reshape clinical practice by delivering meaningful enhancements in therapeutic outcomes.

In the present investigation, two original resin formulations intended for VAT photopolymerization-based 3D printing were developed. These were built upon ternary blends of PEGDA 250, PEG 400, and water, selectively loaded with either AuNSs or AuNRs, with the overarching goal of achieving wavelength-selective drug elution driven by laser exposure at 532 nm and 1064 nm. The experimental workflow commenced with the preparation of the nanoparticulate systems, succeeded by confirmatory characterization of their colloidal robustness and morphological attributes. A mixed-centered experimental design was subsequently applied to identify the

compositional space that maximized the solubilization of the chosen model therapeutic. Guided by this design strategy, three candidate matrices were shortlisted that offered satisfactory Niclosamide solubility while spanning a deliberately broad range of photocurable monomer content, thereby permitting an evaluation of their respective printability.

The 3D-printing trials demonstrated that materials formulated according to Matrix 6 (90% PEGDA 250) exhibited enhanced optical opacity, superior dimensional congruence with the digital template, and improved mass uniformity across replicate prints. Comprehensive physicochemical profiling of the cured constructs validated the effective entrapment of the nanoparticulate fillers, as evidenced by the measurable photothermal response upon laser illumination. Thermal analysis by DSC and TGA confirmed the absence of any degradation phenomena arising from the irradiation step. Furthermore, it was established that the matrices displayed negligible passive leakage of the bioactive payload in the absence of the optical trigger. The subsequent evaluation of stimulus-responsive drug discharge reinforced the critical role of nanoparticle loading density in modulating the kinetics of liberation.

To summarise, from the array of designed matrices, it can be inferred that an operational composition window was successfully delineated, in which the active compound could be adequately dissolved, the blends were amenable to fabrication via VAT photopolymerization, and gated control over active-agent release from the resultant constructs was achieved. Looking ahead, it will be essential to precisely define the boundaries of this formulation space to expand the palette of printable matrices, potentially incorporating alternative photopolymers such as PEGDA 575 and PEGDA 750. Upcoming challenges will include establishing a versatile platform capable of accommodating multiple therapeutic agents and nanoparticulate species that respond across distinct irradiation bands. In certain instances, achieving larger absolute release quantities for less potent drug candidates will be warranted. Moreover, rigorous evaluation of material cytocompatibility remains an indispensable prerequisite to guarantee that the engineered device is fit for safe and efficacious pharmaceutical application.

Acknowledgments: None

Conflict of Interest: None

Financial Support: D.A.R. and M.K. received funding from Agencia Nacional de Investigación y Desarrollo (ANID), Chile: Fondecyt Postdoctoral 3200384 and 3220587, Fondap 15130011 and 1523A0008A. D.A.R., J.P.R., B.B., and S.P. gratefully acknowledge the Universidad Nacional de Córdoba (Argentina) and CONICET (Argentina) for financial support. Fondecyt 1211482, 1201962. Anillo ANID-ACT210059. Fondequip 170111 and Fondequip 160175.

Ethics Statement: None

References

1. Stewart K, Johnston J, Matza L, Curtis S, Havel H, Sweetana S, et al. Preference for pharmaceutical formulation and treatment process attributes. Patient Prefer Adherence. 2016;10:1385-99.
2. Menditto E, Orlando V, De Rosa G, Minghetti P, Musazzi U, Cahir C, et al. Patient centric pharmaceutical drug product design—The impact on medication adherence. Pharmaceutics. 2020;12:44.
3. Vinaud MC, Real D, Fraga CM, Lima NF, De Souza Lino Junior R, Leonardi D, et al. Nanodelivery of nitazoxanide: Impact on the metabolism of Taenia crassiceps cysticerci intracranially inoculated in mice. Ther Deliv. 2020;11:329-39.
4. Roger E, Lagarce F, Garcion E, Benoit JP. Biopharmaceutical parameters to consider in order to alter the fate of nanocarriers after oral delivery. Nanomedicine. 2010;5:287-306.
5. Andrés Real D, Gagliano A, Sonsini N, Wicky G, Orzan L, Leonardi D, et al. Design and optimization of pH-sensitive Eudragit nanoparticles for improved oral delivery of triclabendazole. Int J Pharm. 2022;617:121594.
6. Real D, Formica ML, Picchio ML, Paredes AJ. Manufacturing techniques for nanoparticles in drug delivery. In: Drug Delivery Using Nanomaterials. Boca Raton (FL): CRC Press; 2021. p. 23-48.
7. Tiwari PM, Vig K, Dennis VA, Singh SR. Functionalized gold nanoparticles and their biomedical applications. Nanomaterials. 2011;1:31-63.

8. Maleki Dizaj S, Alipour M, Dalir Abdolahinia E, Ahmadian E, Eftekhari A, Forouhandeh H, et al. Curcumin nanoformulations: Beneficial nanomedicine against cancer. Phytother Res. 2022;36:1156-81.
9. Shrestha B, Tang L, Romero G. Nanoparticles-mediated combination therapies for cancer treatment. Adv Ther. 2019;2:1900076.
10. Chandrakala V, Aruna V, Angajala G. Review on metal nanoparticles as nanocarriers: Current challenges and perspectives in drug delivery systems. Emergent Mater. 2022;5:1593-615.
11. Nejati K, Dadashpour M, Gharibi T, Mellatyar H, Akbarzadeh A. Biomedical applications of functionalized gold nanoparticles: A review. J Clust Sci. 2022;33:1-16.
12. Mustafa DE, Yang T, Xuan Z, Chen S, Tu H, Zhang A. Surface plasmon coupling effect of gold nanoparticles with different shape and size on conventional surface plasmon resonance signal. Plasmonics. 2010;5:221-31.
13. Kogan MJ, Olmedo I, Hosta L, Guerrero AR, Cruz LJ, Albericio F. Peptides and metallic nanoparticles for biomedical applications. Nanomedicine. 2007;2:287-306.
14. Wang J, Zhang HZ, Li RS, Huang CZ. Localized surface plasmon resonance of gold nanorods and assemblies in the view of biomedical analysis. Trends Anal Chem. 2016;80:429-43.
15. Bansal SA, Kumar V, Karimi J, Singh AP, Kumar S. Role of gold nanoparticles in advanced biomedical applications. Nanoscale Adv. 2020;2:3764-87.
16. Guerrero AR, Hassan N, Escobar CA, Albericio F, Kogan MJ, Araya E. Gold nanoparticles for photothermally controlled drug release. Nanomedicine. 2014;9:2023-39.
17. Chia HN, Wu BM. Recent advances in 3D printing of biomaterials. J Biol Eng. 2015;9:4.
18. Lopez-Vidal L, Real DA, Paredes AJ, Real JP, Palma SD. 3D-printed nanocrystals for oral administration of the drugs. In: Drug Delivery Using Nanomaterials. Boca Raton (FL): CRC Press; 2021. p. 109-33.
19. Lopez-Vidal L, Real JP, Real DA, Camacho N, Kogan MJ, Paredes AJ, et al. Nanocrystal-based 3D-printed tablets: Semi-solid extrusion using melting solidification printing process (MESO-PP) for oral administration of poorly soluble drugs. Int J Pharm. 2022;611:121311.
20. Xu X, Awad A, Robles-Martinez P, Gaisford S, Goyanes A, Basit AW. Vat photopolymerization 3D printing for advanced drug delivery and medical device applications. J Control Release. 2021;329:743-57.
21. Robles Martinez P, Basit AW, Gaisford S. The history, developments and opportunities of stereolithography. In: 3D Printing of Pharmaceuticals. Berlin: Springer; 2018. p. 55-79.
22. Popal M, Volk J, Leyhausen G, Geurtsen W. Cytotoxic and genotoxic potential of the type I photoinitiators BAPO and TPO on human oral keratinocytes and V79 fibroblasts. Dent Mater. 2018;34:1783-96.
23. Real DA, Bolaños K, Priotti J, Yutronic N, Kogan MJ, Sierpe R, et al. Cyclodextrin-modified nanomaterials for drug delivery: Classification and advances in controlled release and bioavailability. Pharmaceutics. 2021;13:2131.
24. Real JP, Real DA, Lopez-Vidal L, Barrientos BA, Bolaños K, Tinti MG, et al. 3D-printed gastroretentive tablets loaded with niclosamide nanocrystals by the melting solidification printing process (MESO-PP). Pharmaceutics. 2023;15:1387.
25. Vigderman L, Zubarev ER. High-yield synthesis of gold nanorods with longitudinal SPR peak greater than 1200 nm using hydroquinone as a reducing agent. Chem Mater. 2013;25:1450-7.
26. Salazar Sandoval S, Cortés-Adasme E, Gallardo-Toledo E, Araya I, Celis F, Yutronic N, et al. β-Cyclodextrin-based nanosponges inclusion compounds associated with gold nanorods for potential NIR-II drug delivery. Pharmaceutics. 2022;14:2206.
27. Elbadawi M. Polymeric additive manufacturing: The necessity and utility of rheology. In: Polymer Rheology. London: InTech; 2018.
28. Zanon M, Cue-López R, Martínez-Campos E, Bosch P, Versace DL, Hayek H, et al. Bioderived dyes-mediated vat photopolymerization 3D printing of chitosan hydrogels for tissue engineering. SSRN Electron J. 2022;69:103553.
29. Alketbi AS, Shi Y, Li H, Raza A, Zhang T. Impact of PEGDA photopolymerization in micro-stereolithography on 3D printed hydrogel structure and swelling. Soft Matter. 2021;17:7188-95.
30. Takayama I, Katayama A, Terakawa M. Fabrication of hollow channels surrounded by gold nanoparticles in hydrogel by femtosecond laser irradiation. Nanomaterials. 2020;10:2529.
31. González-Henríquez CM, Pizarro G del C, Sarabia-Vallejos MA, Terraza CA, López-Cabaña ZE. In situ-preparation and characterization of silver-HEMA/PEGDA hydrogel matrix nanocomposites: Silver inclusion studies into hydrogel matrix. Arab J Chem. 2019;12:1413-23.

32. Auclair N, Kaboorani A, Riedl B, Landry V. Acrylated betulin as a comonomer for bio-based coatings. Part I: Characterization, photo-polymerization behavior and thermal stability. Ind Crops Prod. 2015;76:530-7.
33. Pelletier H, Belgacem N, Gandini A. Acrylated vegetable oils as photocrosslinkable materials. J Appl Polym Sci. 2006;99:3218-21.
34. Palucci Rosa R, Rosace G, Arrigo R, Malucelli G. Preparation and characterization of 3D-printed biobased composites containing micro- or nanocrystalline cellulose. Polymers. 2022;14:1886.
35. dos Santos RL, de Sampaio GA, de Carvalho FG, Pithon MM, Guênes GM, Alves PM. Influence of degree of conversion on the biocompatibility of different composites in vivo. Quintessenz J. 2014;16:15.